Automatic image analysis and morphology of fibre reinforced concrete

Carl Redon [a,b], Liliane Chermant [a], Jean-Louis Chermant [a,*], Michel Coster [a]

[a] *LERMAT, UPRESA CNRS 6004, ISMRA, 6, bd. Maréchal Juin, 14050 Caen Cedex, France*
[b] *LRM2C, ESITC Caen, 1, rue Pierre et Marie Curie, 14610 Epron, France*

Abstract

Automatic image analysis is an efficient tool to quantify the morphology of materials. Moreover, it can aid to understand their mechanical behaviour. Several applications of automatic methods are presented to investigate concrete reinforced by ribbon shaped amorphous cast iron fibres. Introducing ribbons into the plain matrix entrapped air voids. This affected the workability and, later on, the compressive strength of the fibre reinforced concrete (FRC). Both were improved by additions of superplasticizer in order to keep the water to cement ratio constant. The influence of the superplasticizer and fibre contents on the compactness of the FRC was characterized by the dimensional and the spatial distributions of the air voids. The orientations of fibres and microcracks were quantified by Fourier image transforms. Due to the casting procedure of the FRC, the fibres were located in "horizontal layers", perpendicular to the casting axis. Whatever the direction of compression with respect to the layers of fibres, the microcrack network was getting more and more oriented in the direction of compression as stresses increased. The analysis of fibre and microcrack orientations suggests that, under uniaxial compression, the inelastic strain domain should be characterized by an anisotropic biaxial damage model, whose principal axes are the orthogonal and parallel directions to the layers of fibres. © 1999 Published by Elsevier Science Ltd. All rights reserved.

Keywords: Automatic image analysis; Fibre reinforced concrete; Amorphous cast iron fibres; Air voids; Fourier transform; Fibre and microcrack orientation; Anisotropy; Mechanical modelling; Workability; Compactness; Strength

1. Introduction

Presently, to increase the strength characteristics of materials – ceramics, concrete, metals and their alloys, etc. – requires a control as accurate as possible of the morphology of their particles, and of their homogeneity. In that way, the methods of automatic image analysis and of mathematical morphology have already become familiar in many research and development laboratories, for example in material science, in biology, but few in civil engineering.

On the one hand, via a digitization of the image, they can replace manual methods to determine the mean parameters of the stereology with a more statistic point of view (mean grain size, mean free path, volumic or surface area, contiguity) [1–3], or compute rose of directions, or roses of intercepts, used to characterize the anisotropy [4,5]. They are set up more rapidly and allow to perform a great number of measurements to get a statistical value in a given accuracy. On the other hand, manual methods do not always permit a complete description. Only computer treatment of digitized images allows the researcher (i) to determine anisotropic properties quickly, via the Fourier transform [6], (ii) to calculate really statistically size distributions, (iii) to implement functions such as the covariogram, the distance function to investigate the dispersion and homogeneity of materials, etc. [7–10]. Moreover, for interconnected networks analysis, the size distributions and the covariograms require absolutely the use of morphologic tools, accessible only by computer treatments [8–10]. These developments have provided not only automatic but also a better statistic quantification of the morphology of bulk materials, and also of damages that materials can undergo. They offer a new tool of investigation, very important for the mechanicians [11,12].

* Corresponding author. Tel.: +33-2-31-452-664; fax: +33-2-31-452-660.

In the case of concrete materials, many morphological parameters of concrete have already been measured by manual or semi-automatic methods in the past decades. The Delesse's method, using the notion of surface area and published in 1848, can be used for that purpose [13]. For example, the ASTM standard proposes to use the Rosiwal's method of direct secants (published in 1898) to measure the pore characteristics [14,15]. Full morphological investigations of concrete, conducted on thin cuts, polished sections or X-ray radiographs, have already been published in the international literature in the past 30 years [16–19]. But they rarely made use of automated methods and mathematical morphology to perform image analysis. Thus, this paper does not pretend to demonstrate the importance of morphological measurements for the concrete knowledge, and it is beyond the scope of the present work to review all these previous studies. But the examples given in the next paragraphs indicate that from now on, computer based automatic image analysis measurements should be preferred whenever possible.

As a typical example, in this research work, the morphology of a concrete matrix reinforced with amorphous cast iron fibres was investigated by automatic image analysis methods. The only objective of this paper is to present how these general automated measurement methods were used to correlate the morphological aspects of a fibre reinforced concrete (FRC), to its mechanical behaviour under uniaxial compression, in terms of strength, possible anisotropy and damage. The morphological investigation was limited at a scale where features are detectable with the eye. At this scale, it was essentially the influence of the morphology of entrapped air voids, fibres and cracks, on the mechanical properties which could be investigated.

The fibre properties, the concrete composition and the casting procedure are described first. Techniques are presented that are similar to those developed in the last decades to prepare the material's samples for image acquisition. Even more than in the case of manual analysis methods, achieving a good sample preparation is a major requirement to conduct correct automatic image analysis measurement. Introducing fibres in a fresh concrete matrix, without adapting the composition to this new constituent, leads to a loss of workability and air voids can be entrapped. Once hardened, this affects the compactness of the material and its corresponding compressive strength. However, workability can be restored by additions of superplasticizer. Usual automatic image analysis treatments can be used to quantify the variations in dimensional and spatial distributions of these air voids. Investigating the air void morphology is then a direct way to characterize the compactness and understand the strength variation as a function of fibre and superplasticizer content.

Fourier image transform was applied to quantify orientations of lines materializing either microcracks or fibres. Such a measurement provides a fast image treatment. It is also quite independent of the digitization artefacts, which were due to the discrete nature of the square grid of the analyser. Comments on all these orientation measurements are finally collected to illustrate, and/or to suggest which model to adopt for the mechanical behaviour of the FRC submitted to uniaxial compression, when the material undergoes inelastic strains.

2. Elaboration of the FRC

The composition of the plain concrete matrix was: 425 kg/m^3 of CPJ CEM II/A 32.5R Portland cement, 890 kg/m^3 of 6/10 mm crushed gravel, 890 kg/m^3 of 0/4 mm rolled washed sand. All these parameters were kept constant. Indeed, this study intends to assess separately the effect of two variables only: the fibre volume fraction and the superplasticizer content.

The amorphous cast iron fibres used to reinforce the plain concrete matrix were 30 mm long, 1.6 mm wide, and 0.03 mm thick. They were metallic glass ribbons fabricated by a melt spinning process. Their main characteristics were: high specific surface area, about 10 m^2/kg, high resistance to corrosion, and tensile strength of 1400–2300 MPa [20,21]. A 0.5% volume fraction (i.e. 36 kg/m^3) of amorphous cast iron fibre was used [22,23].

The polymelamine superplasticizer content – given by the dry mass of superplasticizer per mass of cement – was increased from 0% up to 1%, to assess the optimal workability and strength. For the water to cement ratio (w/c) chosen here, 0.4, this content was optimum around 0.4% (i.e. liquid content = 4.25 kg/m^3) for the plain matrix and for the FRC as well (cf. Fig. 6). The corresponding workability is quantified by a flowing time of 6–8 s in the 40 l vibrating LCL apparatus [24]. Two $450 \times 450 \times 450$ mm^3 FRC cubes were cast with this optimized composition. They were submitted to vibration parallel to the casting axis, during 50 s.

3. Experimental procedures

To characterize the material properties of a FRC, the morphological measures should not be influenced by the wall effects along the sides of the mold. Fibres are for example oriented differently near the walls or the bottom of the specimens [25]. That would not be representative of the bulk material itself, but of the molding procedure. For this study the concrete sections were sawn in the central parts of the concrete blocks (Fig. 1).
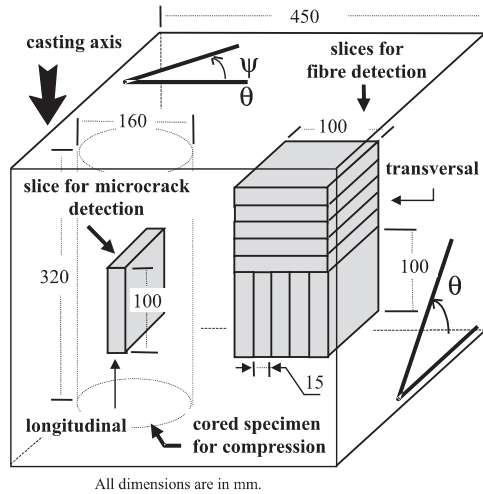
All dimensions are in mm.

Fig. 1. Scheme of a FRC cube and location of the sections observed for the measurement of fibre and microcrack orientation.

3.1. Detection of the air voids

Small concrete slices, about 40×40 mm^2, were polished under water, using diamond grids. The regular polishing facilities limited their size. Each section was blackened with ink, and the air voids were filled with a white paste to achieve good contrast [23,26]. A 33.5×29.0 mm^2 analysis field is presented in Fig. 2. The longest distances between the air voids were on average four times smaller than the specimen's side length. The biggest air voids, below 10 mm in diameter for the poorly compacted FRCs, could be fully included in the field. Despite the small specimen size, this allowed to measure the size and spatial distribution of the air voids.
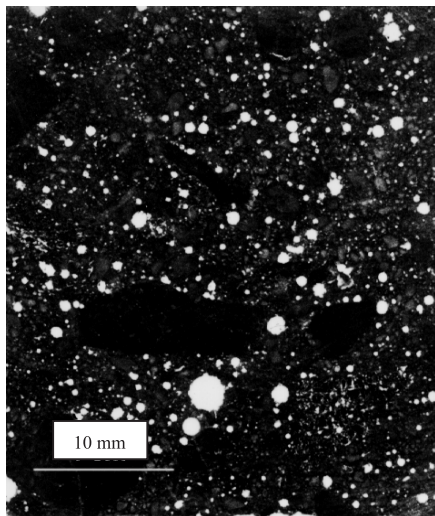
3.2. Detection of the fibres

To detect fibre orientation, five longitudinal and five transversal slices, 15 mm thick, were sawn in the FRC cubes. Their surface was 100×100 mm^2. This ensured that measurements are performed on observation fields which are representative of the heterogeneity of the FRC. Generally such a size corresponds to a representative element of surface area for a plain concrete [27]. This also ensures that the fibres were fully included in the analysis field, as they were 30 mm long.

Without any specific preparation, the slices were placed under a medical X-ray source (Fig. 1) [19,23,28]. In image A, the concrete is visualized in grey and the air voids, in black, are surrounded by thin fibres, in white (Fig. 3).

Such a 2D image is the result of the projection in the direction of the camera of the fibre arrangement in the volume of hardened concrete. However, as the intensity of the X-ray source was limited, it was difficult to achieve a good contrast and to threshold these images automatically.

Although specific filters can be developed to extract the contours of the fibres – such as Laplacian filters [3] – the best visible fibres were traced off manually on transparent films. Fibres, viewed as packed on the projected 2D X-ray images, were materialized by a number of distinguishable lines depending on the importance of the bundles. The traces of the fibres materialized by one pixel large skeletonized lines [3,10] are presented in image B (Fig. 4).
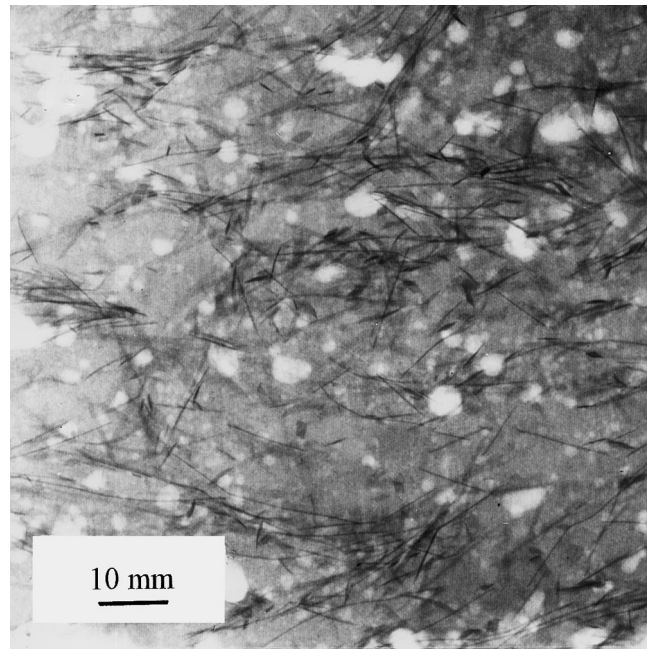

Fig. 2. Detection of the air voids in a non-reinforced concrete matrix section, with 0.2% of superplastcizer.

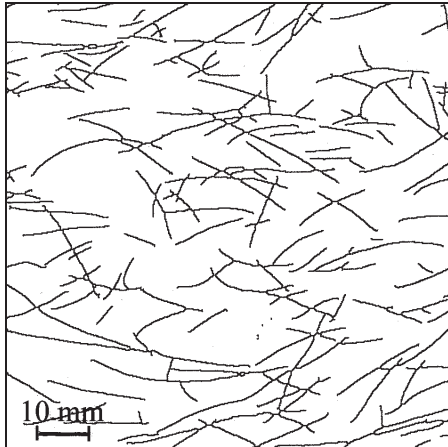Fig. 3. Digitized, 100×100 mm^2, grey level X-ray image A of a longitudinal 15 mm thick FRC slice.

Fig. 4. Digitized image B of the traces of the fibres redrawn from image A.

3.3. Detection of the microcracks

Eight 160 $\varnothing$ ×320 mm³ cylinders were cored in the direction of the casting axis in the FRC blocks ($\theta = 90°$) (Fig. 1). Each FRC cylinder was submitted to uniaxial compression, in the direction of the casting axis. After unloading, only one longitudinal FRC slice, with dimensions 100×100 mm², was cut off vertically in the middle part of each cylinder. Each slice corresponds to a given applied strain level.

These eight slices were then impregnated in low vacuum conditions for 1 h, with a fluorescent epoxy resin. The sections of these specimens were straightened and polished under water, using high rotating speed (1500 rpm) oscillating diamond grids. Similarly to the Forrester's method [29] – spray of oil containing fluorescent particles – used by the team of Stroeven at Delft University of Technology [17,30], here the fluorescence of the resin in the pores and the cracks was revealed under UV light [31]. Visible microcracks, roughly larger than 100 μm, have been manually drawn on transparent films for different strain levels (Fig. 5(a)–(c)).

3.4. Image acquisition and treatment

The images of the air voids, fibres and microcracks, were all acquired with a black and white CCD camera. The corresponding video images were digitized on the discrete square grid, 512×512 pixels in size, of an automatic image analyser – Morpho Pericolor 3100 Matra MS2I (St Quentin en Yvelines, France). They were then thresholded to get binary images.

4. Compression strength and morphology of the air voids

Due to the fact that concrete exhibits a wide size distribution of air voids, the chosen magnification did not allow detection of pores smaller than 3 pixels in diameter (i.e. 206 μm). Moreover, smaller air voids are more closely related to the microstructure of the fresh cement paste. Thus, they are less likely to give information on the loss of compactness due to a loss of workability.

For samples having the same superplasticizer content, the tests confirmed that the compressive strength of the FRC at 28 days was lower than the plain concrete matrix's one. Rossi [32] has already observed that the use of this ribbon fibre does not lead to higher concrete compressive strengths. But increasing the superplasticizer amount, up to an optimum content, close to 0.4%, enhanced the FRC strength from 40 up to 45 MPa, and that of the concrete matrix from 38 up to 53 MPa (Fig. 6). A larger increase caused strength degradation as also observed by Gagne et al. [22,33], for high strength-concrete containing no silica fume.

4.1. Granulometry of the air voids

To assess freeze-thaw durability, pore analysis has been conducted on concrete, even by automatic approaches, for many years [26,34]. In the present study, only the effect of air voids on the compressive strength was investigated. For the plain concrete matrix and
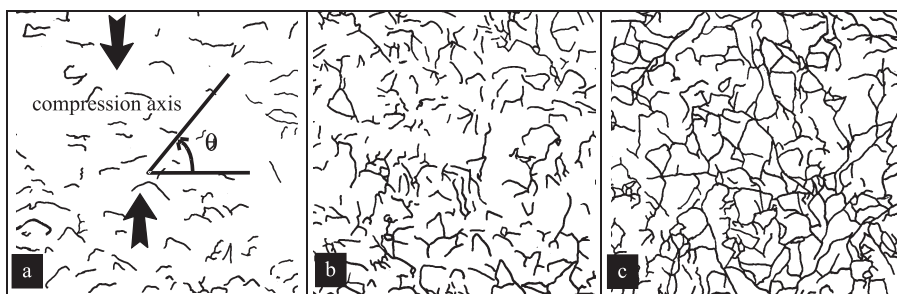

Fig. 5. Microcrack pattern for increasing axial compression strains, ε, visualized on 100×100 mm² sections: (a) $\varepsilon = 1.5 \times 10^{-4}$; (b) $\varepsilon = 9.6 \times 10^{-4}$; (c) $\varepsilon = 1.9 \times 10^{-3}$.
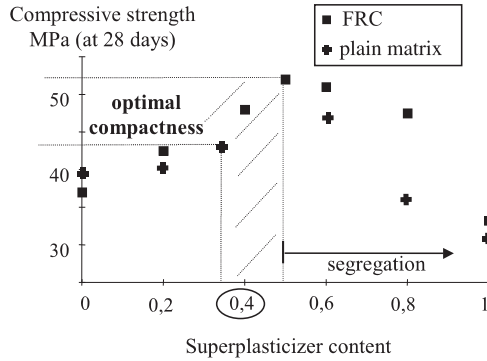
Fig. 6. Change in compressive strength as a function of fibre content and of superplasticizer content (% of dry mass of superplasticizer per mass of cement), for a concrete matrix and for a FRC.

Fig. 8. Granulometry in measure: total surface area occupied by the air voids as a function of their diameter for 0.2% of superplasticizer, and for air voids larger than 206 μm.

FRC investigated here, two types of air void size distributions were established as a function of the superplasticizer and fibre contents. If the total number of pixels corresponding to a given size is numbered, a granulometry in number is obtained (size distribution). But, if the total surface area occupied by all the air voids of a given size is measured, it defines a granulometry in measure corresponding to a weighted granulometry [3,10].

By automatic image analysis, the surface of an air void can be measured: it corresponds to a number of pixels. The size of a pixel corresponded here to 68.5 μm. Both granulometries were performed on twenty-seven 33.5×29.0 mm^2 observation fields.

The granulometry in number reveals that the number of large air voids, whose diameter is greater than 1.5 mm, is negligible in the concrete matrix and in the FRC too. It also reveals that the number of air voids is larger in the concrete matrix than in the FRC (Fig. 7). However, in the case of the matrix, the granulometry in measure indicates that a major part of the total air void surface area corresponds to small voids (Fig. 8).

Conversely, in the case of the FRC, the total surface occupied by large air voids is as important as that corresponding to air voids whose diameter is less than 1.5
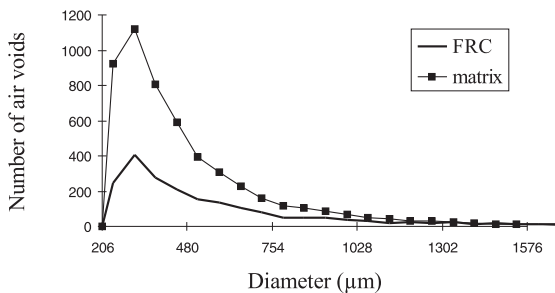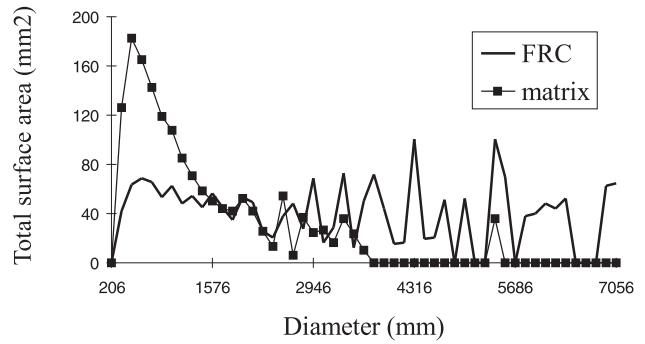
mm. The trend is the same for superplasticizer contents ranging from 0% up to 0.4%.

The surface fraction of the air voids, $A_a(V)$, was also calculated. It corresponds to the total surface area of the air voids divided by the surface of the 27 observation fields. The air void surface area fraction was not much larger in the FRC (Table 1), than in the concrete matrix [$A_a(V) = 9.7\%$, for 0% superplasticizer content; $A_a(V) = 6.2\%$, for 0.2%; $A_a(V) = 4.2\%$ for 0.4%]. The number of air voids per cm^2, N_a, has also been averaged on these 27 observation fields for the FRCs (Table 1). It is always lower than the one measured on the matrix samples having similar superplasticizer contents [$N_a(V) = 21$, for 0%; $N_a(V) = 19$, for 0.2%; $N_a(V) = 13$, for 0.4%].

When fibres were introduced in the fresh concrete matrix, the observed strength loss was due to a loss of compactness. Indeed, the macroporosity of the FRC mainly consisted of large air voids, which were not present in the plain concrete matrix [23,35].

4.2. Distance between the air voids

By automatic image analysis, using a distance function algorithm, the percentage of the solid phase of concrete (i.e. hardened cement paste, gravel, sand and

Fig. 7. Granulometry in number: number of air voids as a function of their diameter, for 0.2% of superplasticizer, and for air voids larger than 206 μm.

Table 1
Mean distance, $\bar{r}$, between the air voids larger than 200 μm, and its corresponding standard deviation, $\bar{\sigma}$, number of air voids per cm^2, $N_a(V)$, and surface fraction of the air voids, $A_a(V)$, in FRC as a function of the superplasticizer content, s%

Superplasticizer content	0%	0.2%	0.4%
$\bar{r}$ (mm)	0.97	1.28	1.40
$\bar{\sigma}$ (mm)	0.76	0.90	0.96
$\bar{\sigma}/\bar{r}$	0.78	0.70	0.68
$N_a(V)$	13	8	9
$A_a(V)$	12.00	6.80	5.40

fibres) located at a given distance, r, from surrounding dispersed individual air voids in IR^2 can be measured [3,22,36]. The distance function is a distribution function where the parameter is the distance rather than the size. From this distance function, it is possible to compute the mean value, $\bar{r}$, the standard deviation, $\bar{\sigma}$, and also the normalized standard deviation, $\bar{\sigma}/\bar{r}$, for several superplasticizer contents (Table 1).

If the superplasticizer content increases to 0.4%, the mean distance between the air voids is enhanced and the normalized standard deviation decreases. The increasing value of $\bar{r}$ can be explained geometrically by the decreasing values of A_a and N_a. The decrease of $\bar{\sigma}/\bar{r}$ corresponds to a more regular dispersion of air voids, not in the sense of a Poisson's process, but with an equilibrium between "attraction and repulsion process in air void interaction". So, these measurements on the hardened material suggest that a correct adjustment of the superplasticizer content provided a better compactness. With the aid of all these morphological parameters, whose values were obtained by automatic image analysis methods, it appears now that the compactness can be directly quantified, as opposed to indirectly estimated, for example by compression tests.

5. Fourier image transform to measure orientations of lines

5.1. Artefacts of the digitalization

The rose of direction measurement corresponds to a function, $L_2(X, \alpha)$, which gives, in polar coordinates, the length of the contours of an object X, oriented in the direction $\alpha \pm d\alpha$ (Fig. 9) [3,10]. All orientations α are achievable in continuous space, but not in the discrete space which is defined on the square grid of the analyser. Consider the example of a 14° actual direction. As a result of the digitization artefacts, this line is discretized in small joined 0° segments.

Usual rose of direction algorithms are based on a hit or miss process based on the configuration of 3- or 5-pixels long structural elements. But at the 3×3 pixels
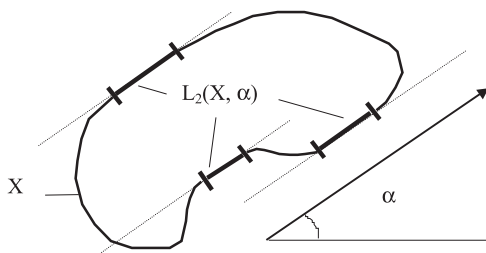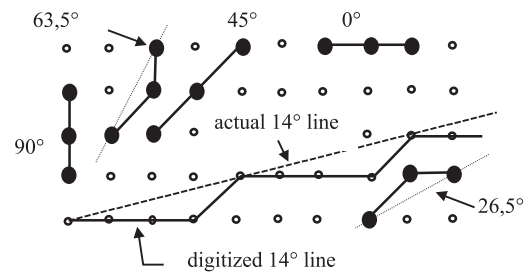

Fig. 10. Discrete square grid of the analyser: structural elements which can be defined at the 3×3 pixels scale (in black), and digitization artefacts for an actual 14° line.

scale, only 0°, 45°, 90°, ±26.5° and ±63.5° orientations can be detected (Fig. 10) [3,10,37]. In that case, the 14° orientation will be quantified as a succession of very local 0° directions. To detect an actual 14° orientation, either longer structural elements have to be used, which would be an intermediate solution, or the image should be considered at a global level, that is to say at the 512×512 pixels scale. In this last case, the angular precision can be as accurate as arctg (1 pixel/512 pixels) $\approx 0.11°$. This is achievable by the Fourier image transform [6,23,38].

5.2. The discrete fourier image transform

The discrete Fourier transform $X(u, v)$, of a grey level image defined by a bidimensional function, $x(k, l)$, is a complex image:

$$X(u,v) = \frac{1}{N} \sum_{k,l=0}^{N-1} x(k,l) \times e^{-(2i\pi/N) \times (uk+vl)} \tag{1}$$

for $u, v = 0, \ldots, N - 1$; and N corresponding to the image width given by a number of pixels (here $N = 512$).

Defined in the discrete frequency domain, the Fourier spectrum of image B (Fig. 4) is presented in Fig. 11(a). This new grey level image reveals the anisotropy of the fibre orientation in image B. Indeed, the highest grey levels are located in a 60–120° angle. As the Fourier transform induces a $\pi/2$ shift from real to frequency domain, the fibres in image B are oriented in the ±30° range. For example, the detection of the portions of fibres in the 20° direction is obtained by the convolution product with the mask $H(u,v)$ oriented at 110° (Fig. 11(b)). This mask is centred on the middle of the spectrum and its length is limited to the low frequencies corresponding to the fibre representation in the Fourier domain. Its width is determined depending on the accuracy required for the quantification of the orientation, here ±5°. It was not possible to achieve such an accuracy at the 3×3 pixels scale. The inverse Fourier transform, $y(k, l)$ is operated by the convolution product:

Fig. 9. Illustration of the principle of the rose of directions to measure $L_2(X, \alpha)$.
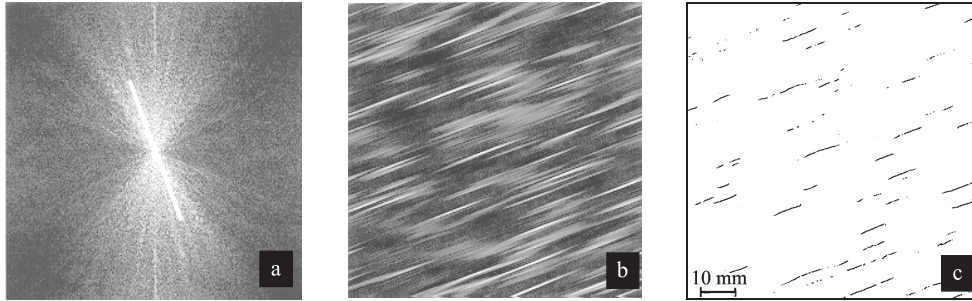
Fig. 11. (a) The Fourier spectrum of image B; the 110° convolution mask is drawn in white; (b) the inverse Fourier transform of (a); (c) the 20° portions of fibres detected by the Fourier transform algorithm on image B.

$$y(k, l) = \frac{1}{N} \sum_{u,v=0}^{N-1} X(u,v) \times H(u,v) \times e^{(2i\pi/N) \times (uk+vl)}. \qquad (2)$$

The white traces in the inverse Fourier transform image reveals the portions of fibres of image B which are in the 20° direction (Fig. 11(b)). These traces are thresholded and the inverse Fourier transform image is then intersected with image B. Thus, all the portions of fibres aligned in the 20° direction are isolated (Fig. 11(c)). The mask $H(u,v)$ has been rotated every 10°, to get an accurate rose of directions of the fibres.

5.3. Fibre orientations in the hardened FRC

In the past decades, many publications have dealt with the quantification of fibre orientation [19,28]. But the researcher should refer to Debicki's work dealing with orientation measurements of the identical ribbon shaped amorphous cast iron fibres reinforcing a mortar [39]. The same tendency is observed for the concrete investigated in this work. The fibre orientation, ψ, is approximately isotropic in the 2D projected images of the transversal sections, which are perpendicular to the casting axis (Fig. 12(a)). However, the fibre orientation is highly anisotropic in the projected images of the longitudinal planes, parallel to the casting axis. All fibres are located in a $\theta = \pm 30°$ angle (Fig. 12(b)).

The gravity forces of the concrete falling, and the vibrations during the casting, tend to align the fibres in "horizontal layers" perpendicular to the casting axis. Indeed, fibres are very sensitive to gravity as they are ribbon shaped and as their specific surface area is important. The layers of amorphous ribbons tend to prevent air extraction during the vibration. As seen on X-ray images, this can lead to the formation of large horizontal flat air voids surrounded by the fibres.

5.4. Microcrack orientation as a function of compression strain

Cracking, in compression or in tension, has been studied extensively by image analysis in plain concrete and FRC materials [17,40]. The microcracks' morphology has even been investigated by automatic methods which were also generally making use of the concept of the total projection and of the rose of intercepts [4,41–43]. In the case of the FRC investigated here, the use of the Fourier transform revealed that the contribution of the $\theta = 90°$ microcracks increases with the strain level. Conversely the length of the $\theta = 0°$ microcracks remains approximately constant (Fig. 13). It is clearly apparent that the microcracking process is more and more anisotropic, being oriented in the direction of the compression (Fig. 14(a)–(c)) [23].
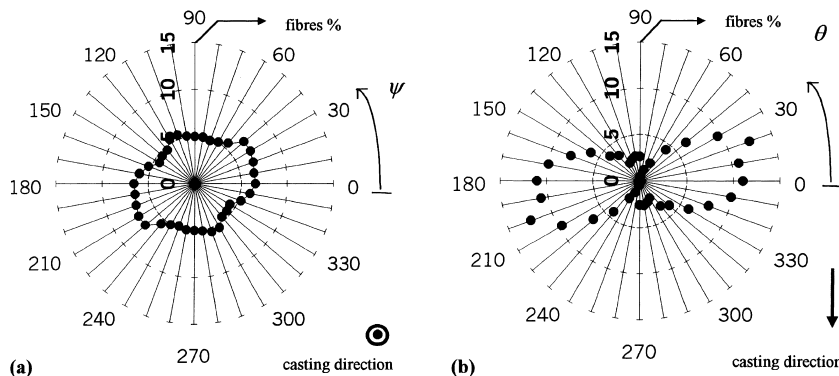

Fig. 12. Mean fibre orientation measured in five transversal (a) and in five longitudinal (b) FRC slices (see Fig. 1).
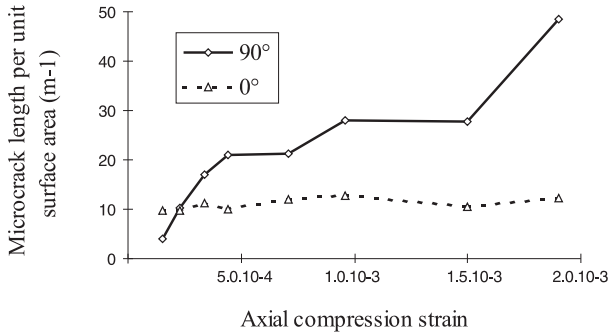
Fig. 13. Evolution of the $\theta = 0°$ and $90°$ microcrack length per unit surface area (given in m^{-1}) as a function of the compression strain.

In a non-reinforced concrete matrix, both direct observations on sections and X-rays or ultrasonic methods have revealed that microcracking develops axially, mainly in the direction of compression [44–46]. The same trend is observed for the FRC investigated here. The global microcrack orientation is not considerably deviated by fibres arranged in perpendicular horizontal ($\theta = \pm 30°$) layers. A complementary investigation showed that if compression was applied in a direction parallel to the layers of fibres, the final microcrack orientation was also mainly parallel to the compression axis [23]. This confirms Debiki's research on failure modes in a mortar reinforced with the same fibres. Whenever the FRC was stressed in a direction parallel or perpendicular to the layers of fibres, he had noticed that the failure cracks were running in the direction of compression. Conversely, he observed that a shear mode failure occurred when the compression axis was inclined about $\theta = 60°$ to the fibre layers [39].

6. Discussion on anisotropic damage in compression

The 3D spatial arrangement of the fibres in the FRC is said to be isotropic transverse. This means that it is close to a laminate system. It is isotropic within the layers of fibres and has a revolution axis, which corresponds here to the casting axis. Transverse isotropy means that a symmetry of revolution is defined around this axis [23,39].

As the fibre spatial arrangement is isotropic transverse, since flat horizontal air voids surrounded by fibres may be encountered, it should imply that the FRC stiffness will be different following the casting axis or the "layers" of fibres. Thus, the stiffness matrix A_0, relating elastic strains, ε_{ei}, to the compression stresses, σ_i, which is also isotropic transverse, should be written under the form [27]:

$$
\begin{pmatrix} \varepsilon_{e1} \\ \varepsilon_{e2} \\ \varepsilon_{e3} \end{pmatrix} = \begin{pmatrix} \frac{1}{E_1} & \frac{-v_{21}}{E_2} & \frac{-v_{21}}{E_2} \\ \frac{-v_{21}}{E_2} & \frac{1}{E_2} & \frac{-v_{32}}{E_2} \\ \frac{-v_{21}}{E_2} & \frac{-v_{32}}{E_2} & \frac{1}{E_2} \end{pmatrix} \begin{pmatrix} \sigma_1 \\ \sigma_2 \\ \sigma_3 \end{pmatrix}, \tag{3}
$$

with $i = 1$, and 2, or 3, respectively in the direction of the casting axis, and in two orthogonal directions perpendicular to the casting axis, $E_{1,2}$, respectively, the Young modulus in the direction 1 or 2 (or 3), v_{21}, and v_{32}, the Poisson coefficients.

However, compression tests have revealed that the stiffness matrix of this FRC was isotropic in the elastic strain domain [23]. Thus, the anisotropic morphology does not always imply an anisotropic mechanical behaviour. It can be understood that a fibre volume fraction as low as 0.5% is not likely to influence any elastic parameters.

But as soon as microcracking takes place in the FRC, the material undergoes inelastic strains. The mechanics of concrete failure has been a wild topic of research in the past decades [47,48]. In the present work, the compressive strength degradation was investigated by the concept of damage mechanics firstly introduced by Katchanov [49]. Sidoroff and then Benouniche [50,51]
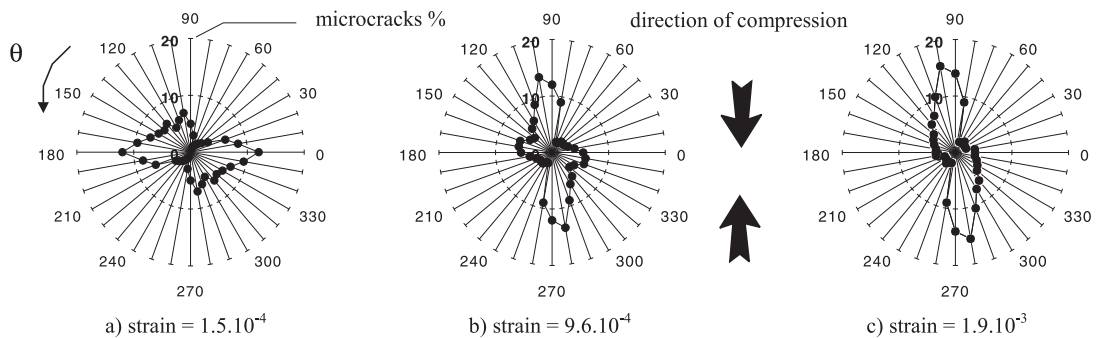

a) strain = $1.5.10^{-4}$ b) strain = $9.6.10^{-4}$ c) strain = $1.9.10^{-3}$

Fig. 14. Microcrack orientation, θ, in longitudinal sections as a function of increasing compression strain, from (a) to (c).

modelled damage microcracking of plain concrete under uniaxial compression, by stating that the original A_0 stiffness matrix is modified into a new $A(A_0, D)$ stiffness matrix function of the damage variable D. As mentioned in Section 5.4, microcracking is becoming anisotropic as the strain increases. D should then be written as a diagonal matrix defined by two components: d_1 in the direction of compression and d_2 in any radial direction, perpendicular to that axis (Eq. (4)). The evolutions of these two damage variables are to be measured, by mechanical tests, to quantify the loss of stiffness of the FRC as strain is increased:

$$D = \begin{pmatrix} d_1 & 0 & 0 \\ 0 & d_2 & 0 \\ 0 & 0 & d_2 \end{pmatrix}. \tag{4}$$

In the inelastic strain domain, in fact, it was observed that the decrease of stiffness was greater and faster when the FRC was compressed in a direction parallel to the planes of fibres. Fibre/matrix debonding occurred by microcraking in the direction of the compression, in the weak interface transition zones around the fibres. On the contrary, the loss of stiffness was delayed when the FRC was compressed in the direction of the casting axis [23,52]. In that case, fibres located in a $\theta = \pm30°$ sector delayed the predominant $\theta = 90°$ microcracking process.

7. Conclusion

The objective of this paper is to show that today it is possible to use automatic image analysis methods to get access to information about mechanical behaviour and modelling of materials. Such automated methods are suitable to investigate civil engineering materials, as has also recently been illustrated in a publication of Nemati et al. [43]. Such information confirms all the previous morphological parameters measured manually or semi-automatically by many authors. In the present case, the morphology of a concrete reinforced with amorphous cast iron fibres (ribbons) was quantified to investigate its mechanical behaviour under uniaxial compression.

The quantification of the macroporosity has revealed that the introduction of fibres in the concrete matrix lead to the formation of large entrapped air voids. This loss of compactness explained why the measured compression strength of the plain concrete matrix was generally higher than the FRC one. However, the compactness was partially recovered by the use of an optimum superplasticizer amount, about 0.4%. For this content, indeed, the distance between the air voids was increased.

In such an optimized amorphous cast iron fibre reinforced concrete, the fibre 3D arrangement was isotropic transverse. The nearly horizontal orientation of the fibres, in a direction perpendicular to the casting axis, was evidenced by the 2D Fourier image transform. As this method is not sensitive to the digitization artefacts, it is well suited to determine the orientations of a line pattern on the discrete square grid of the automatic analysers.

Similarly, axial microcrack anisotropy was apparent, being oriented in the direction of the compression.

It appeared that the loss of stiffness of the FRC is anisotropic, depending on the direction in which uniaxial compression is applied. Thus, only in the inelastic strain domain, the mechanical behaviour could be related to morphological features, essentially with regard to fibre and microcracking orientation.

References

[1] De Hoff RT, Rhines FN. Quantitative microscopy. New York: McGraw-Hill, 1968.

[2] Underwood EE. Quantitative stereology. Reading, MA: Addison Wesley, 1970.

[3] Coster M, Chermant JL. Précis d'analyse d'images. 2nd ed. Les Presses du CNRS, 1989.

[4] Ringot E. Automatic quantification of microcrack network by stereological method of total projection in mortars and concretes. Cement Concr Res 1988;18:35–43.

[5] Nemati KM, Stroeven P. Fracture analysis of concrete: a stereological approach. Proceedings of the Third International Conference on Fracture Mechanics of Concrete Structures, Proc. FRAMCOS-3, AEDIFICATIO, Gifu, Japan, 12–16 October 1998, 47–56.

[6] Redon C, Chermant L, Chermant JL, Coster M. Assessment of fibre orientation in reinforced concrete, using Fourier image transform. J Microscopy 1998;191(3):258–65.

[7] Matheron G. Les variables régionalisées et leur estimation. Paris: Masson, 1965.

[8] Haas A, Matheron G, Serra J. Morphologie mathématique et granulométrie en place. Ann Mines 1967;11:736–53.

[9] Haas A, Matheron G, Serra J. Morphologie mathématique et granulométrie en place. Ann Mines 1967;12:767–82.

[10] Serra J. Image analysis and mathematical morphology. New York: Academic Press, 1982.

[11] Henault E, Coster M, Chermant JL. Grain-boundary reconstruction by automatic image-analysis on etch pits. Mat Res Bull 1991;26(7):569–75.

[12] Boitier G, Chermant JL, Chermant L, Doreau F, Vicens J. Morphologie par analyse d'images de composites à fibres longues: principes et résultats. Rev Met CIT Sci Génie Mat 1997;94:1517–36.

[13] Delesse, Procédé mécanique pour déterminer la composition des roches. Ann Mines 1848;13:379.

[14] Rosiwal A. Uber geometrische Gesteinsanalysen; ein einfacher Weg zur ziffermässigen Feststellung des Quantitätsverhältnisses des mineralbestandteile gemengter Gesteine. Verhandl KK, Geol Reichsanst, Vienna, 1898;5–6:143.

[15] Hoover KC. Air content and unit weight of hardened concrete. In: Klieger P, Lamond JF, editors. Significance of tests and properties of concrete making materials, ASTM STP 169C 1994;296–314.

[16] Hsu TTC, Slate FO, Sturman GM, Winter G. Microcracking of plain concrete and the shape of the stress–strain curve. ACI J 1963;60(2):209–24.

[17] Stroeven P. Some aspects of the micromechanics of concrete. Ph.D. Thesis, TU Delft – University of Technology, The Netherlands, 1973.

[18] Stroeven P, De Hann YM. Structural investigations on steel fibre concrete by stereological methods. In: Reinhardt HW, Naaman AE, Spon E & FN, editors. Proceedings of the 15th International RILEM Symposium on ACI Workshop High Performance Fibre Reinforced Cement Composites. London:Chapman & Hall, 1992:407–18.

[19] Kasperkiewicz J, Malmberg B, Skarendahl A. Determination of fibre content, distribution and orientation in steel fibre concrete by X-ray technique. Proceedings of RILEM Symposium on Testing and Tests Methods of Fibre Cement Composites, Sheffield, UK. Lancaster:The Construction Press, 1978:297–314.

[20] De Gillebon B, Shom JM. Metallic glass ribbons – a new fibre for concrete reinforcement. In: Developments in fibre reinforced cement and concrete. University of Sheffield. Proceedings of RILEM Symposium, vol. 12, 1986.

[21] Brandt AM. In: Spon E& FN, editor. Cement-based composites, materials, mechanical properties and performance. 1st ed. London:Chapman & Hall, 1995.

[22] Redon C, Quenec'h JL, Chermant L, Chermant JL. Influence of superplasticizer and metallic glass ribbons on the macroporosity and the compressive strength in concrete. Acta Stereol 1996;15:233–9.

[23] Redon C. Morphologie et comportement mécanique de bétons renforcés par des fibres de fonte amorphe. Thèse de Doctorat of the University of Caen, France, 1997.

[24] Baron J, Lesage R. Pour une étude pratique de la maniablité: le maniabilimètre Lesage du Laboratoire Central des Ponts et Chaussées. Bull Liaison LCPC 1965;13.

[25] Stroeven P. Stereology of concrete reinforced with short steel fibres. Fract Mech Struct Aspects Concr 1986;31:15–28.

[26] Chatterji S, Gudmundsson H. Characterization of entrained air bubble systems in concrete by means of an image analysing microscope. Cement Concr Res 1977;7:423–8.

[27] Lemaitre J, Chaboche J. Mécanique des matériaux solides, 1988.

[28] Stroeven P, Shah SP. Use of radiography-image analysis for steel fibre reinforced concrete. Proceedings of RILEM Symposium on Testing and Tests Methods of Fibre Cement Composites, Sheffield, UK. Lancaster: The Construction Press, 1978:345–53.

[29] Forrester JA. Discussion: propagation and detection of cracks under short- and long-term loading. In: Brooks AE, Newman K, editors. Proceedings of the International Conference on The Sructure of Concrete and its Behaviour Under Load, London, UK, September 1965. Cement and Concrete Association, 1965:154–65.

[30] Stroeven P. Some observations on microcracking in concrete subjected to various loading regimes. Eng Fract Mech 1990;35:775–82.

[31] Kawamura M, Igarashi S. Application of the fluorescence microscopic technique to the sudy on the propagation of cracks in cement paste and mortar. In: Brandt AM, Li VC, Marshall IH, editors. Proceedings of the International Symposium on Brittle

Matrix Composites 4, Warsaw, Poland, 13–15 September 1994. IKE and Woodhead Publ., 167–76.

[32] Rossi P. Steel fibre-reinforced concretes (SFRC) – An example of french research. ACI Mat J 1994;91(3):273–9.

[33] Gagne R, Boisvert A, Pigeon M. Effect of superplasticizer dosage on mechanical properties, permeability and freeze-thaw durability of high-strength concretes with and without silica fume. ACI Mat J 1996;93(2):111–20.

[34] Wilk W, Dobrolubov G, Romer B. Development in quality control of concrete during construction. Transportation Research Record, 53rd Annual Meeting of Highway Research Board, vol. 504. Washington, DC: National Research Council, 1974:1–26.

[35] Redon C, Chermant L, Chermant JL, Quenec'h JL. Characterization of the macroporosity of concrete using an automatic image analysis. In: Brandt AM, Li VC, Marshall IH, editors. Proceedings of the Internationational Symposium on Brittle Matrix Composites 5, Warsaw, Poland, 13–15 October 1997. Cambridge/Warsaw:Woohead Pub. Ltd/Bigraf, 1997:291–99.

[36] Redon C, Chermant L, Coster M, Chermant JL, Quenec'h JL. Sur la mesure de distances inter-bulles sur des sections de bétons par analyse d'images. Bull Liaison LCPC 1997;211:25–32.

[37] Chaix JM, Grillon F. On the rose of directions measurements on the discrete grid of an automatic image analyser. J Microscopy 1996;184:208–13.

[38] Gonzalez LM, Cumbrera F, Sanchez-Bajo F, Pajares A. Measurement of fibre orientation in short-fibre composites. Acta Metall Mater 1994;42:689–94.

[39] Debicki G. Contribution à l'étude du rôle de fibres dispersées anisotropiquement dans le mortier de ciment sur les lois de comportement. Les critères de résistance et la fissuration du matériau. Thèse de Doctorat of the INSA of Lyon and of the University Claude Bernard Lyon I, France, 1988.

[40] Saito M. Characteristics of microcracking in concrete under static and repeated tensile loading. Cement Concr Res 1987;17:211–8.

[41] Carcasses M, Ollivier JP, Ringot E. Analysis of microcracking in concrete. Acta Stereol 1989;8/2:307–12.

[42] Stang H, Mobasher B, Shah SP. Quantitative damage characterization in polypropylene fibre reinforced concrete. Cement Concr Res 1990;20:540–58.

[43] Nemati KM, Monteiro PJM, Scrivener KL. Analysis of compressive stress-induced cracks in concrete. ACI Mat J, Technical Paper 1998;95(5):617–30.

[44] Slate FO, Olsefski S. X-ray study of internal structure and microcracking of concrete. J Am Concr Inst 1962;60:575–88.

[45] Robinson GS. Methods of detecting the formation and propagation of microcrack in concrete. Cement Concr Assoc 1968:131–45.

[46] Stroeven P. Geometric probability approach to the examination of microcracking in plain concrete. J Mat Sci 1979;14:1141–51.

[47] Vile GWD. Behaviour of concrete under simple and combined stresses. Ph.D. Thesis, University of London, London, UK, 1965.

[48] Mc.Greath DR. Fracture mechanics of concrete. Ph.D. Thesis, Imperial College, London, UK, 1968.

[49] Katchanov L. Rupture time under creep conditions. Izv Akad Nauk SSSR, OTN 1958;8:26–31.

[50] Sidoroff F. Description of anisotropic damage application to elasticity. In: Hult J, Lemaître J, editors. Symposium IUTAM, Physical Non Linearities in Structural Analysis, May 1980, Senlis, France. J Phys Appl Mech 1980:237–44.

[51] Bénouniche S. Modélisation de l'endommagement du béton hydraulique par microfissuration en compression. Thèse de 3ème Cycle of the University of Paris VI, Fance, 1979.

[52] Redon C, Chermant JL. Damage mechanics applied to concrete reinforced with amorphous cast iron fibres, Concrete subjected to compression. Cement Concr Comp 1999; 21:197–204.